Applied Acoustics 254 (2026) 111430

Contents lists available at ScienceDirect

Applied Acoustics

journal homepage: www.elsevier.com/locate/apacoust

Machine learning-enabled fast determination of vibroacoustic response using sub-structuring and patch-based approach

Jingjie Dong, Rendong Pi, Hangxing Li, Li Cheng, Xiang Yu *

Department of Mechanical Engineering, The Hong Kong Polytechnic University, Hung Hom, Kowloon 999077, Hong Kong SAR China

ARTICLE INFO

Keywords:
Vibro-acoustic analysis
Coupling
Sub-structuring approach
Transfer learning

ABSTRACT

Predicting the vibro-acoustic responses of complex systems is important for engineering noise control, yet it remains challenging when system geometries and boundary conditions are complicated or difficult to estimate. To address this issue, we propose a transfer learning aided patch transfer function (TL-PTF) method which retains the flexibility of the conventional PTF framework while substantially reducing the workload required to characterize complex sub-systems. To characterize a sub-system for which analytical solutions are not available, we first train a neural network using transfer functions from a standard sub-system with similar modal characteristics. Then, this network is fine-tuned using only a small amount of data obtained directly from the target, complex sub-system. This two-stage strategy enables accurate characterization while substantially reducing the required data-collection workload. The transfer functions predicted by the transfer learning neural network are subsequently incorporated into the PTF framework for coupling analysis. The workflow of the proposed TL-PTF method is demonstrated on a representative plate–cavity system and validated numerically and experimentally for cases with different excitations and boundary conditions. With appropriate sampling strategies, the effort required to acquire PTFs can be reduced to approximately 1/7 of that needed for conventional PTF methods, while still maintaining acceptable prediction accuracy. The proposed framework provides a systematic and efficient methodology for vibro-acoustic response prediction in complex systems, with strong potential for practical applications such as cabin noise prediction and control in aircraft and high-speed trains.

1. Introduction

Vibro-acoustic systems composed of elastic plates and acoustic cavities are widely seen in engineering applications, including simplified cabin models for air vehicles, submarines and high-speed trains. The low-frequency noise generated by the interaction between plate vibrations and the internal acoustic field is a major concern, as it can directly affect passengers' comfort, operational efficiency and safety. Consequently, vibroacoustic analyses of these coupled systems are essential for developing effective noise control strategies [1–3].

Early research on vibro-acoustic analysis of plate-cavity systems primarily relied on modal-based methods [4–6], which are limited to simple geometric configurations. Subsequently, numerical methods such as the finite element method (FEM) and the boundary element method (BEM) [2,7,8], as well as energy-based approaches [9,10], have been widely applied to such coupled problems. Researchers are continuously developing methods and strategies to predict the response of complex coupled systems that are difficult to handle using conventional techniques. For example, Li and Cheng [11,12] proposed a combined integro-modal method to analyze the coupling characteristics between a vibrating plate and a cavity with a tilted wall. Fritze et al. [13] proposed a FEM-BEM coupling method for shell-geometry sensitivity analysis to avoid non-matching meshes. Xuan et al. [14] extended the finite volume method (FVM) to analyze the transient response and natural characteristics of fluid-filled structural–acoustic coupling systems. Xie et al. [15] developed a unified method for three-dimensional coupling systems using the weak form variational-based method (VBM). Additionally, an improved B-spline wavelet-based method (WBM) was proposed and proved to be more stable with non-uniform meshes [16]. However, most of the published methods remain limited to relatively simple cavity configurations and boundary conditions.

The Patch Transfer Function (PTF) method has been established in the past decade as an effective tool for analyzing structural–acoustic coupled systems [17], offering high flexibility and computational efficiency. As a sub-structuring technique, transfer functions are defined based on the mean values of physical quantities on *patches* – small

* Corresponding author.
E-mail address: lucien.yu@polyu.edu.hk (X. Yu).

https://doi.org/10.1016/j.apacoust.2026.111430
Received 8 December 2025; Received in revised form 23 April 2026; Accepted 8 June 2026
Available online 12 June 2026

elements discretized on the coupling surfaces. The patch transfer functions (PTFs) are pre-determined and are subsequently utilized for interface matching. A key feature of the PTF approach is that sub-system PTFs can be obtained from analytical [18–21], numerical [17,22,23] and experimental [24,25] methods, allowing for flexible and versatile modeling. While the PTF method offers an accurate and flexible framework for vibro-acoustic analysis, it faces significant computational challenges when the system dimension, complexity, and frequency increase. Specifically, the workload required for PTF measurements increases quadratically with system size or frequency range. What's more, the experimental methods for measuring the PTF of acoustic cavities are still not fully developed [25]. Consequently, modeling and analyzing complex vibro-acoustic systems using the PTF method remains challenging.

In recent years, deep learning approaches have gained significant attention in engineering analyses, particularly in performance prediction [26–31], structural design [32–38] and parameter identification [39], showcasing their transformative potential to enhance computational efficiency. Lee and Park [40] first applied deep learning techniques in transfer path analysis, and later, Lee [41] proposed a deep learning approach trained on operational response measurements and known joint stiffness to indirectly estimate the frequency response function of a single structure, which provides a potential link between physical modeling and machine learning. However, in most cases, deep learning models are used to establish direct mappings between design variables and dynamic responses. While this strategy is convenient for prediction, it restricts the model's applicability to new but highly similar problems, since a new dataset is needed to train each new model. Moreover, obtaining sufficient high-quality datasets without compromising computational efficiency remains a major challenge. In this context, transfer learning shows promise in reducing the required dataset size by training target models based on knowledge learned from previous tasks [42–44]. This approach not only mitigates the need for extensive data collection but also accelerates the model training process, making it feasible to tackle diverse engineering challenges with improved adaptability and speed.

In this study, we propose a patch-based approach for rapid prediction of coupling responses in structural–acoustic systems. To improve both efficiency and generalizability, a neural network model is employed to predict sub-system transfer functions. With the aid of transfer learning, the neural network for the target system can be trained with a limited amount of data. The outputs from transfer learning models are then incorporated into the PTF framework to predict the dynamic response of the global system. The effectiveness of the approach is validated through a thin plate backed by a polygonal cavity. The transfer learning neural network is constructed using data from a few test points inside and on the surface of the acoustic cavity. The predicted coupling responses agree well with simulation and experiment results in both the frequency and spatial domains. Compared with conventional numerical and analytical techniques, the present method achieves fast and accurate vibro-acoustic coupling predictions using only a small dataset and is applicable to systems with different boundary conditions and excitations, offering higher efficiency than the traditional PTF method. This work provides a generalized computational framework for vibro-acoustic coupling analysis without the need for modal information.

The paper is structured as follows. Section 2 briefly outlines the framework of the PTF method. Section 3 introduces the proposed method. Section 4 presents the prediction results and discussions. Section 5 summarizes the main conclusions.

2. PTF method

This section describes the general steps for solving the vibro-acoustic coupled problem using the PTF method, illustrated with a simple plate–cavity system. First, the coupled system is decomposed into several sub-systems, and the PTFs on the connected interfaces are defined. Second, the patch velocities at the interfaces are solved by applying coupling conditions. Third, other coupled responses within the coupled system are computed using the coupling velocities obtained before. More complicated systems are modeled and solved in a similar manner.

2.1. Sub-system decomposition

The structural–acoustic system consists of a flexible plate backed by an acoustic cavity, as illustrated in Fig. 1(a). The thin plate with dimensions $L_x \times L_y$ and thickness t is simply coupled to the surface Γ_s of the air cavity. The structural–acoustic coupled system is excited by a point source S, and the vibrating velocity V_s of the point source is assumed to be unity. The remaining surfaces of the cavity, denoted as Γ_a, are assumed to be acoustically rigid. This structural–acoustic system effectively represents typical cabin environments. A listening point L is placed inside the acoustic cavity to measure the acoustic response. The locations of the source point S and the listening point L are shown in Fig. 1. As a sub-structuring approach, the PTF method firstly divides the coupling system into sub-systems (cf. Fig. 1(b)): Ω_s, representing the flexible plate, and Ω_a, representing the air cavity [17]. In this context, the surface Γ_s between structural sub-system Ω_s and acoustic sub-system Ω_a is defined as the coupling interface. Subsequently, the coupling interface is partitioned into small patches, which serve as the minimum calculation units.

A *priori* characterization is performed by calculating the PTFs for each sub-system, which describe the relationship of forces and velocities between different patches. In this study, we assume harmonic excitations and thus omit the explicit time dependence $e^{j\omega t}$ in the analysis, where j denotes the imaginary unit and ω is the angular frequency.

For the structural sub-system, the PTFs are defined as mobilities, calculated as the ratio of the mean normal velocity on a listening patch i to the mean pressure applied on an excitation patch j:

$$Y_{ij} = \frac{\langle V \rangle_i}{\langle P \rangle_j}, \tag{1}$$

where $\langle \cdot \rangle$ denotes the area average value: $\langle f \rangle_P = \frac{1}{A_P}\int_{S_P} f(y,z)\mathrm{d}S$ and A_p is the area of S_P; V and P denote the normal velocity and excitation pressure, respectively. Similarly, the PTFs for the acoustic sub-system are defined as impedances, determined by the ratio of the mean sound pressure on a listening patch i to the mean velocity of an excitation patch j:

$$Z_{ij} = \frac{\langle P \rangle_i}{\langle V \rangle_j}. \tag{2}$$

For a coupled system with an internal point source of vibrating velocity V_s, the patch-to-point transfer functions are defined as the ratio of the mean sound pressure on a listening patch i to the velocity of the excitation source point S:

$$\widetilde{Z}_i = \frac{\langle P \rangle_i}{V_S}. \tag{3}$$

For any listening point inside the coupling system, the surface integral in Eq. (1)-(3) reduces to the corresponding point value.

2.2. Interface matching

After sub-system characterization, the PTF assembly for the coupled system can be performed based on the linearity properties of the system [17]. For the cavity Ω_a, the patch pressures are expressed as the sum of the initial blocked patch pressures $\widetilde{P}$ before coupling, and the pressures induced by the plate vibration:

$$\langle P \rangle_i = \left\langle \widetilde{P} \right\rangle_i + \sum_{j=1}^{N} Z_{ij} \langle V \rangle_j, \tag{4}$$

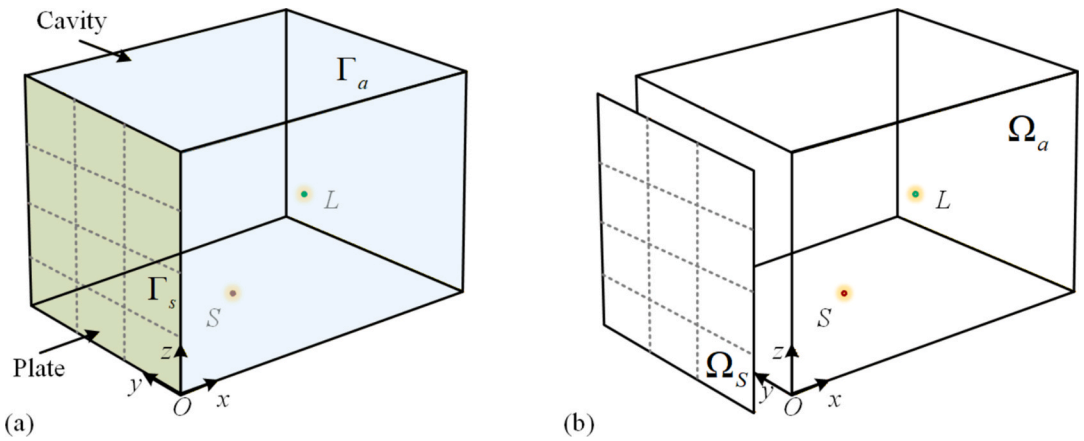

Fig. 1. (a) Sketch of the structural–acoustic system; (b) Sub-system division.

where N is the number of patches.

The patch velocities of the plate Ω_s can be expressed as a sum of the initial velocities $\widetilde{V}$ before coupling, and the velocities resulted from the coupled domain:

$$\langle V\rangle_i = \left\langle \widetilde{V} \right\rangle_i + \sum_{j=1}^{N} Y_{ij}\langle P\rangle_j, \tag{5}$$

where $Y_{i,j}$ denotes the PTFs of the plate defined in Eq. (1), which can be determined using several well-established approaches. By solving the above equations, the coupling patch velocities on the interface Γ_s can be obtained.

2.3. Coupling calculation

Once the velocity of each patch on the connected interface is determined, other coupled responses, such as the sound pressure P_k at the listening point within the coupled system, can be calculated as [45]:

$$P_k = \widetilde{P}_k + \sum_{i=1}^{N} Z_{k,i}\langle V\rangle_i, \tag{6}$$

where $\widetilde{P}_k$ denotes the initial pressure before coupling, while $Z_{k,i}$ denotes the transfer function between the listening point and patch i. Noted that the subscripts in Eq. (4) and Eq. (6) differs slightly, as Eq. (4) refers to the patch sound pressure on the coupling interface, whereas Eq. (6) gives the sound pressure at an arbitrary point within the coupled system.

For the plate-cavity system described in Section 2.1, the blocked patch pressure $\widetilde{P}$ can be calculated as

$$\left\langle \widetilde{P} \right\rangle_i = \widetilde{Z}_i V_s, \tag{7}$$

where $\widetilde{Z}_i$ denotes the transfer function between patch i and the source point. The initial pressure $\widetilde{P}_k$ at the listening point can be calculated as

$$\widetilde{P}_k = \widetilde{Z}_k V_s, \tag{8}$$

where $\widetilde{Z}_k$ denotes the transfer function between the listening point and the source point.

At this stage, all the variables in Eq. (6) can be obtained from the corresponding transfer functions. Following the above procedure yields the dynamic response of the coupled system, which includes all the physical interactions between the vibro-acoustic system. Nevertheless, certain effects, such as the radiated field, resulting from the plate-induced vibrations, are usually omitted as second order contributions [18].

It should be noted that the PTFs are intrinsic properties of the sub-systems and are independent of the initial excitation conditions. This highlights the advantage of the PTF method, as sub-systems can be modeled individually and subsequently coupled with minimal computational effort. In Section 3, a unified neural network model is developed to predict the subsystem transfer functions, which further enhances the practicality and convenience of the PTF approach.

3. Proposed TL-PTF method

Despite the flexibility of the PTF method, rapid prediction of coupling responses remains largely constrained by the computational efficiency of sub-system transfer functions, especially in practical engineering applications where system geometries and boundary conditions are complicated or difficult to estimate. To address this challenge, the transfer learning technique is introduced for predicting the transfer functions of complex acoustic sub-systems, and subsequently integrated in the PTF framework, resulting in the proposed transfer learning aided PTF (TL-PTF) method. This method has proven to be efficient and convenient in situations where analytical solutions for the sub-systems are unavailable.

3.1. TL-PTF method

The procedure for coupling analysis based on the PTF method is summarized in Fig. 2(a). First, the coupled patch velocities are computed based on the actual excitation conditions. Second, the sound pressure of the coupled system is determined based on the relationship established through the transfer functions. In the proposed TL-PTF method, the transfer functions of the cavity are estimated by a neural network, as shown in Fig. 2(b). Transfer learning technique is employed to train the neural network, owing to its high efficiency to perform well with small datasets. Specifically, a neural network is first pre-trained on a large dataset generated for a regular acoustic cavity (*source cavity*), for which analytical solutions are available. The resulting model, denoted as Net-Pre, is then transferred to the cavity of interest (*target cavity*) by initializing a second model, denoted as Net-TL, with the weights and biases of Net-Pre. Importantly, Net-Pre and Net-TL share the same input and output definitions and identical network architecture. This transfer learning technique aims to substantially reduce the amount of training data required for the target cavity while maintaining comparable prediction accuracy, thereby improving both training efficiency and model generalization. Note that the term “source” refers to the previous learning task in the transfer learning setting [46,47], rather than the excitation source in structural–acoustic coupling.

The TL-PTF method is developed under the following assumptions: (1) The patch location is represented by its center coordinates. This simplifies the neural network’s input variables from patch location to

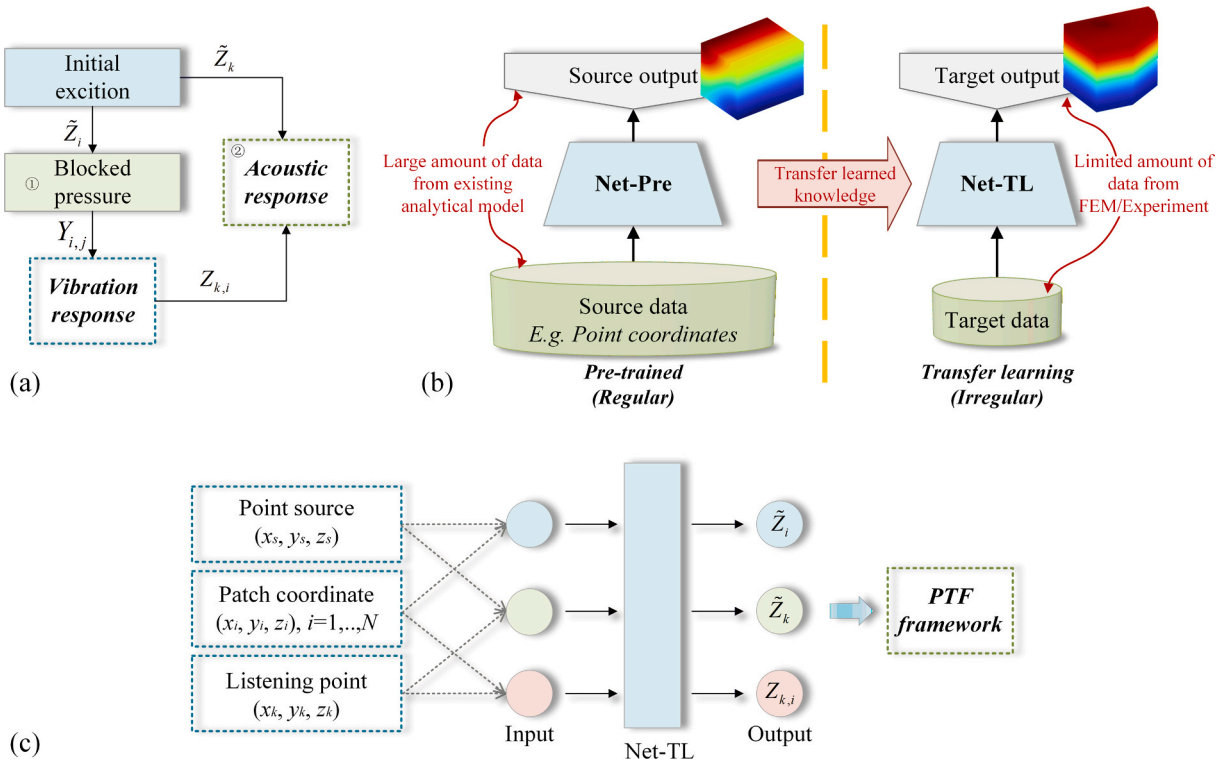

Fig. 2. TL-PTF method for coupling analysis. (a) Calculation procedure of the PTF method; (b) Schematic diagram of the transfer learning model; (c) Flowchart of the TL-PTF method.

point coordinates. The validity of this assumption will be verified in Section 4.1; (2) The acoustic cavities before and after transfer learning should have similar dimensions, as will be further explained in Section 3.2.2.

According to the definition, the transfer functions are determined by the average physical variables on the excitation and listening patches, which were represented by their center point coordinates. Therefore, the input variables of the neural network are defined as the coordinates of the excitation and listening points, and the output variables are the corresponding transfer functions. The source point is located at $\boldsymbol{\xi}_s = (x_s, y_s, z_s)$, the patch centers are located at $\boldsymbol{\xi}_i = (x_i, y_i, z_i)$, and the listening points are located at $\boldsymbol{\xi}_k = (x_k, y_k, z_k)$. The transfer functions to be predicted by the neural network are shown in Fig. 2(c), including $\tilde{Z}_i$ (the transfer function between patch i and the source point), $\tilde{Z}_k$ (the transfer function between the listening point and the source point), and $Z_{k,i}$ (the transfer function between the listening point and patch i). Finally, all the predicted transfer functions are post-processed to obtain the coupling acoustic response within the system, as given in Eq. (5).

The TL-PTF method enables a comprehensive characterization of the coupled system, for which efficient neural network training for transfer function prediction is essential. Accordingly, this study will focus on employing transfer learning techniques to develop a neural network model with high efficiency. The development of the neural network, including dataset preparation and the model framework, will be described in detail in Sections 3.2 and 3.3.

3.2. Dataset preparation

Studies have shown that acoustic cavities with similar dimensions exhibit comparable modal characteristics in corresponding directions [15]. In this section, the pre-trained dataset is generated using the analytical solutions of a rectangular cavity with the same envelope dimensions as the target complex cavity, while the transfer learning dataset is obtained from simulation.

3.2.1. Pre-trained dataset

The dataset for Net-Pre is constructed using the analytical solutions for a rectangular cavity with rigid boundaries, which have been well documented in the literature [18,22]. Accordingly, only a brief derivation is presented here, with the detailed analytical derivations provided in Appendix A.

Consider a rectangular cavity, as depicted in Fig. 1, with dimensions $L_x \times L_y \times L_z$. The sound pressure fields inside the rectangular air cavity can be expressed as a superposition of acoustic modes with modal numbers p, q, $r = 0, 1, 2, \ldots$,

$$p(x,y,z) = \sum_{p,q,r} A_{p,q,r}\varphi_{p,q,r}(x,y,z) = \sum_{p,q,r} A_{p,q,r}\cos(k_x x)\cos(k_y y)\cos(k_z z), \quad (9)$$

where $A_{p,q,r}$ and $\varphi_{p,q,r}$ are the modal amplitude and mode shape function of the eigenmodes, respectively; k_x, k_y and k_z are the wave numbers, given by $k_x = p\pi/L_x$, $k_y = q\pi/L_y$ and $k_z = r\pi/L_z$.

Based on the Green's function and the Helmholtz equation, the transfer function between the excitation point j and the listening patch i writes:

$$Z_{i,j} = -\frac{j\rho\omega}{S_i S_j}\sum_{p,q,r}\frac{\left[\int_{S_i}\varphi_{p,q,r}(x_i,y_i,z_i)\mathrm{d}S\right]\left[\int_{S_j}\varphi_{p,q,r}(x_j,y_j,z_j)\mathrm{d}S\right]}{(k^{*2}-k_{p,q,r}^2)N_{p,q,r}}, \quad (10)$$

where the complex wave number $k^* = \omega/[c\sqrt{1+j\eta_a}]$, with η_a being the damping loss factor associated with the air medium. $k_{p,q,r} = \sqrt{k_x^2+k_y^2+k_z^2}$. The modal mass $N_{p,q,r}$ is

$$N_{p,q,r} = \int_0^{L_x}\int_0^{L_y}\int_0^{L_z}\cos^2(k_x x)\cos^2(k_y y)\cos^2(k_z z). \quad (11)$$

A cavity with outer dimensions measuring around $L_x \times L_y \times L_z = 0.515\ \mathrm{m} \times 0.515\ \mathrm{m} \times 0.7\ \mathrm{m}$ is considered in this study. To ensure accuracy, the modal truncation frequency is set to be twice the maximum computation frequency $f_{\max}$. The studied frequency range is 10 – 800 Hz

with increment range of 5 Hz. The resulting transfer function is expressed as a complex vector of length $L_f = 159$, which contains both real and imaginary components to simultaneously represent the amplitude and phase of the pressure oscillation. To ensure the accuracy and representativeness of the dataset, the sampling interval should be less than 1/6 of the minimum wavelength λ_a, as typically required by element-based methods, where $\lambda_a = c_0 / f_{\max}$. Therefore, the number of sampling points N_s in the source cavity is 640, and the point distribution is summarized in Table 1. For simplicity, the excitation points and the listening points are generated with same space locations. In linear systems, the transfer functions are reciprocal, i.e., $Z_{i,j} = Z_{j,i}$ (see Eq. (7)). As a result, a dataset of size $N_s^2 \times 2$ is established. The dataset is divided into a training set and a test set according to a ratio of 8:2.

3.2.2. Transfer learning dataset

The structural–acoustic coupled system shown in Fig. 3 is used to demonstrate the effectiveness of the TL-PTF method, where a polygonal acoustic cavity approximates the cabin of a transport device. The transfer learning dataset for Net-TL is obtained through simulation using the pressure acoustics module in COMSOL Multiphysics ®. Here, we first consider the target cavity with rigid boundaries to demonstrate the feasibility of transfer learning, as such boundaries maintain clear and well-defined modal characteristics. The discussion regarding different boundaries is also provided in Section 4.3.2. The transfer function is defined as the pressure at the listening point, with a unit velocity at the excitation point. Note that the dataset is constructed using simulations instead of experiments in the first place, as this enables precise adjustment over dataset size and distribution of measuring points for performance analysis. Experimental validations will be provided in later sections.

The geometric dimensions of the irregular acoustic cavity are shown in Fig. 3. The overall envelope dimensions of the irregular cavity are consistent with those of the rectangular cavity. Fig. 4 presents the 2nd, 5th, 8th, and 11th mode shapes for both the source and target cavities. Since the dimension in the z- direction remains unchanged, the corresponding modes (such as the 2nd and 11th) exhibit very similar mode frequencies and mode shapes. The mode frequencies along the x- and y-directions, as well as the coupled modes of the target cavity, are higher due to the reduced effective lengths in these directions. Overall, the two cavities display similar mode shapes but clearly different frequencies, which supports the assumption that the acoustic cavities before and after transfer learning should have similar dimensions.

Since a smaller dataset is expected when using the transfer learning approach, the number of sampling points in the target field is initially set to be 1/10 of that in the original source field. Therefore, the number of the uniformly distributed sampling points N_t in the target cavity is 64, and the transfer learning dataset size is $N_t^2 \times 2$. To evaluate the efficiency of transfer learning, only a subset of the transfer learning dataset is utilized to train Net-TL. The effects of the distributions and numbers of the sampling points will be further discussed in Section 4. The dataset is obtained by sequentially assigning each sampling point as the excitation location and computing the responses at the remaining points to calculate the corresponding transfer functions. That is, for a sub-system with N_t sampling points, the calculation must be repeated N_t times to build the required dataset. Similarly, the transfer learning dataset is partitioned into a training set and a test set according to an 8:2 ratio. In this study, we use a representative cavity configuration to establish a baseline for the TL-PTF method. Extensions to alternative geometries will be investigated in future work.

Table 1
The sampling point distribution of the source cavity.

	Interval	Point number
x-	0.070 m	10
y-	0.064 m	8
z-	0.064 m	8
Total number N_s		640

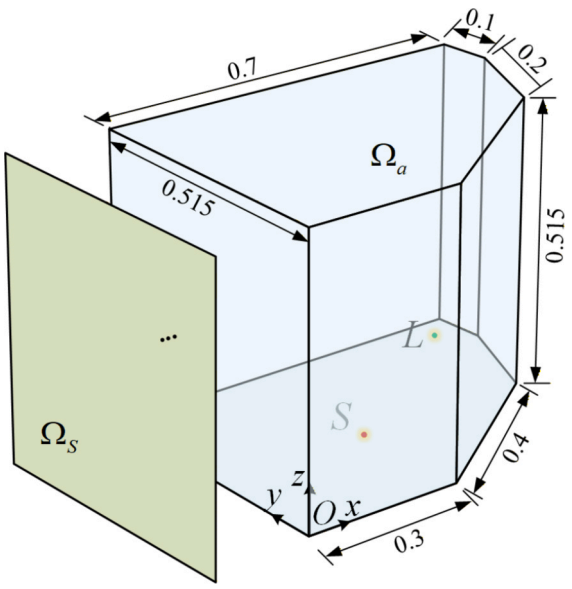

Fig. 3. The schematic diagram of the target field.

3.3. Neural network model framework

Transfer learning is conducted in two stages. In the first stage, Net-Pre is trained using the pre-trained dataset. The developed neural network mainly consists of fully connected (FC) layers, designed to take the point coordinates as input to predict transfer functions. The detailed network architecture is illustrated in Fig. 5, where B denotes the batch size, d_{in} is the input dimension, h_1 and h_2 are the dimensions of hidden layers, and d_{out} is the output dimension. The input variables are processed by three FC blocks. The first two FC blocks use the Leaky Rectified Linear Unit (Leaky ReLU) activation to enable nonlinear feature mapping, while the third FC block uses the hyperbolic tangent (tanh) activation. The FC layers perform feature extraction from the input, and the dropout layers are employed to mitigate overfitting.

The developed model aims to predict the transfer function between an excitation location (x_s, y_s, z_s) and a listening location (x_k, y_k, z_k) in the cavity. Accordingly, the input dimension $d_{in} = 6$. As depicted in Section 3.2, the transfer function is sampled at L_f discrete frequencies, resulting in a complex-valued target vector $\mathrm{H} \in \mathbb{C}^{L_f}$. The real and imaginary parts are concatenated to form the real-valued output:

$$\boldsymbol{y} = [\mathrm{Re}(\mathrm{H}), \mathrm{Im}(\mathrm{H})] \in \mathbb{R}^{2L_f}. \tag{12}$$

Therefore, the output dimension is $d_{out} = 318$, and the neural work model learns the mapping

$$\underbrace{[x_s, y_s, z_s, x_k, y_k, z_k]}_{\in \mathbb{R}^{d_{in}}} \rightarrow \underbrace{\boldsymbol{y}}_{\in \mathbb{R}^{d_{out}}}. \tag{13}$$

The Adam optimizer is employed to optimize the parameters of the neural network. The maximum of training epochs is set as 100 with a batch size B = 16, $h_1 = 1024$, and $h_2 = 256$. Architecturally, the FC layers follow an expansion-and-compression structure. Initially, the d_{in}-dimensional input features are normalized and projected into an h_1-dimensional space, after which the feature dimension is gradually reduced to produce the final d_{out}-dimensional prediction. Fig. 5 illustrates the specific process of feature dimension reduction. Since the real and imaginary parts of the complex vector exhibit different numerical scales, we normalized each part separately with its own scaling parameters, which are then concatenated to form the final training output.

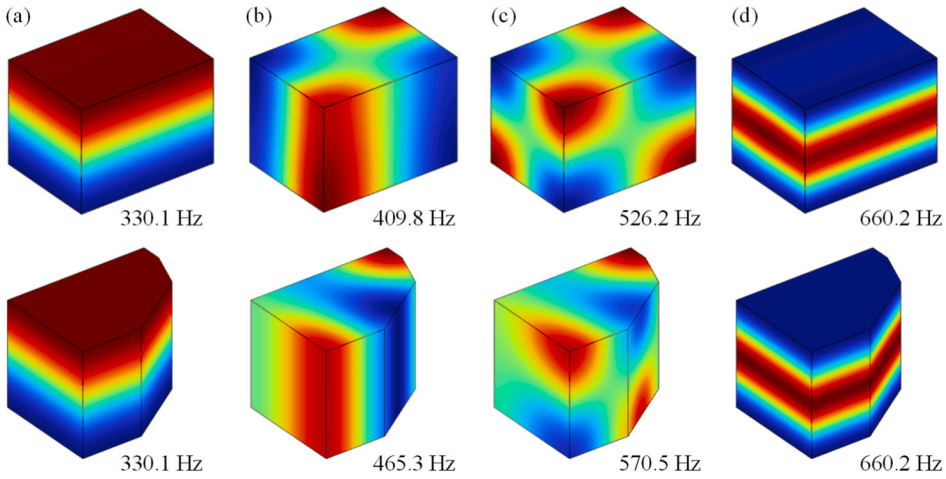

Fig. 4. The mode shapes of the source and target cavities: (a) 2nd; (b) 5th; (c) 8th; (d) 11th modes.

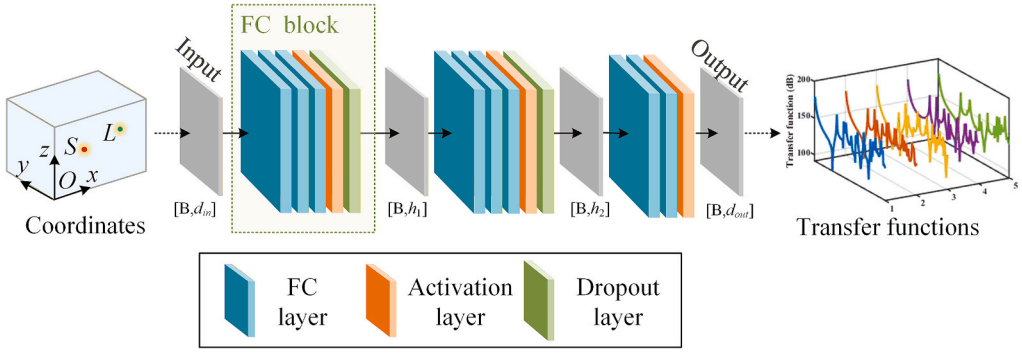

Fig. 5. Architecture of the neural network model.

The normalization procedure may compromise the prediction accuracy at locations far from resonance frequencies, as the significant responses occur at resonance frequencies. However, since the responses at the resonance positions are more concerned with, this normalization approach is considered acceptable.

The loss function is defined as the mean square error (MSE) function writes as

$$\text{Loss} = \frac{1}{N_{batch}} \sum_{i=1}^{N_{batch}} (a_i - b_i)^2, \tag{14}$$

where a_i and b_i denote the ground truth values and predicted values, respectively, and N_{batch} is the number of training batches. Both the real and imaginary parts of the output are considered in the calculation.

In the second stage, we initialize the transfer model Net-TL with the weights of the pre-trained model (Net-Pre) and then fine-tune it on the limited dataset from the target cavity. Net-TL uses the same network architecture and training pipeline as Net-Pre.

4. Results and discussion

In this section, we first analyze convergence to validate the assumptions of the TL-PTF method. Subsequently, the training effect and prediction performance of the transfer learning model are thoroughly investigated. Finally, the established TL-PTF method is validated through systems with different boundary conditions.

4.1. Convergence verification

Previous studies have shown that the patch dimension should be smaller than 1/2 of the minimum wavelength λ_a to guarantee convergence [17,18]. In this study, each patch location is defined by its center coordinates, and the patch-averaged response is approximated by the center value. This treatment differs slightly from previous studies, and it is necessary to examine whether it still satisfies the half-wavelength requirement. The validation was conducted according to the procedure presented in [17]. The rectangular cavity on Fig. 1 is studied and the interface is divided into $N_y \times N_z$ patches, with patch length d_y and d_z, respectively. Table 2 summarizes the patch dimensions and the frequency f_a, defined by the criterion $\lambda_a/2$.

Fig. 6 shows the acoustic impedance $Z_{1,1}$ calculated using 2×2 patches and 3×3 patches, where the solid line represents the approximation result, while the dashed line indicates the actual curve. All results are obtained using the modal expansion method. There is good agreement when the frequency is below f_a, which is also indicated in Fig. 6. Based on these results, it appears that the approach utilized in this study can be applied to the PTF framework.

4.2. Performance analysis of the neural network

A performance analysis is conducted before applying the neural network in the TL-PTF framework. The training effect and prediction performance of both Net-Pre and Net-TL are investigated to validate the

Table 2
Interface patch division.

$N_y \times N_z$	d_y	d_z	f_a
2×2	0.258 m	0.258 m	660 Hz
3×3	0.172 m	0.172 m	990 Hz

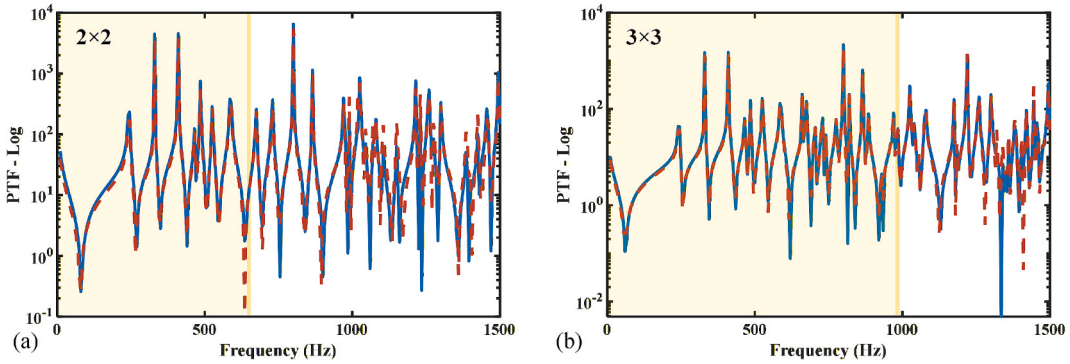

Fig. 6. $Z_{1,1}$ with different numbers of patches. (a) 2 × 2 patches; (b) 3 × 3 patches.

effectiveness of transfer learning for sub-system modelling. The solution process by means of the present approach is implemented in Python 3.10.12.

4.2.1. Net-Pre

Net-Pre is validated prior to transfer learning. The training effect of the model is characterized by calculating the loss iteration during training. The rate at which the loss decreases with each epoch reflects the convergence efficiency of the model. Fig. 7 illustrates the loss iteration during training Net-Pre on the training set and the test set, respectively. The prediction model achieves the most significant reduction in loss after 100 iterations with the lowest loss values of 7.496 × 10^{-5} and 7.629 × 10^{-5}, indicating that the training converged efficiently.

To assess the prediction performance of the Net-Pre, $N_{test} = 902$ sets of unseen data were selected as input variables. The excitation source point is located at (0.25 m, 0.15 m, 0.05 m), while the listening points are uniformly distributed across the surface of the cavity to visualize the acoustic field distribution. The regression coefficient R^2 is calculated to evaluate how effectively Net-Pre captures the variance and overall trend of the sub-system responses, which is defined as

$$R^2 = 1 - \frac{\sum_{i=1}^{N}(a_i - b_i)^2}{\sum_{i=1}^{N}(a_i - \overline{a})^2}, \tag{15}$$

where $\overline{a}$ denotes the average of the ground-truth value. N is the length of the network output. As indicated by the Eq. (15), the closer the R^2 value is to 1, the more accurate the prediction, while providing a quantitative assessment of model performance. The R^2 values are shown in Fig. 8(a), which are generally in the range of 0.985 to 1, showing the high prediction accuracy of Net-Pre.

Assuming the excitation point has a unit velocity, the output corresponds numerically to the sound pressure at the listening points, with a size of $N_{test} \times L_f$. To further illustrate the prediction capability of the source neural network, Fig. 8 also presents the output results for specified locations and frequencies.

The sound pressure level (SPL) at an arbitrarily selected point (0, 0.15 m, 0.15 m) is plotted in Fig. 8(b) as

$$\mathrm{SPL} = 20\log_{10}(p_i/p_{ref}), \tag{16}$$

where $p_{ref} = 2 \times 10^{-5}$ Pa is the reference sound pressure in air. The peaks observed in the SPL curve indicate the resonant frequencies of the acoustic cavity and show good agreement with the ground-truth values in terms of overall trend and distribution.

Furthermore, Fig. 8(c) presents the sound pressure distributions at the first two peaks of the SPL curve, which correspond to the first two resonant frequencies. For comparison, the simulation results at the same frequencies are also provided. Obviously, all the predicted results align well with the ground-truth values, proving that Net-Pre performs well for design-on-demand.

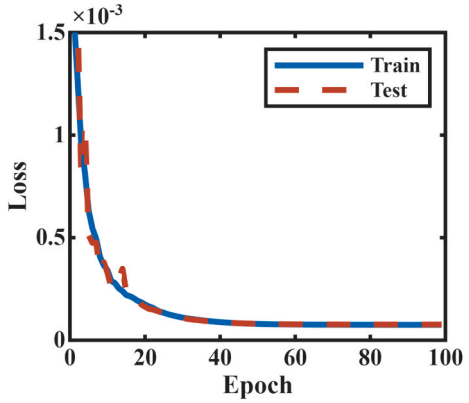

Fig. 7. Iterative plot of the loss during training Net-Pre.

4.2.2. Net-TL

Net-TL is initialized with the training weights of Net-Pre obtained in Section 4.2.1 and subsequently trained on the transfer learning dataset. The number of neurons, as well as other hyperparameters of Net-TL are consistent as well. To demonstrate the ability of transfer learning to accelerate training, we trained a neural network without transfer learning using the entire transfer learning dataset (N), as well as a neural network with transfer learning using half of the transfer learning dataset ($N/2$). Fig. 9 presents the loss comparison of the two neural networks during training. Compared with the neural network without transfer learning, the loss of the transfer learning neural network decreases faster in both the training set and the test set, proving that the transfer learning technique can effectively speed up training. Moreover, only half of the dataset was used for transfer learning neural network, proving that the transfer learning technique can achieve similar training effect with less data required.

Similarly, to verify the prediction performance of Net-TL, $N_{test} = 674$ sets of unseen data are utilized as input variables. The excitation point is in the same location as that in Section 4.1, and the listening points are uniformly distributed with an interval of 0.05 m. The corresponding predicted results are presented in Fig. 10. The R^2 values are basically around 0.9 to 1, and the outputs agree well with that from simulation, proving the prediction effect of Net-TL.

Comparison of Fig. 8 and Fig. 10 shows that, despite geometric differences, the frequency responses and sound pressure distributions are similar in some regions, owing to comparable dimensions along the x-, y-, and z- directions. This further supports the feasibility of transfer learning. Despite using a smaller dataset size, Net-TL performs well in response prediction. In summary, by leveraging pre-trained knowledge from the source cavity, the transfer learning framework reduces the required dataset size and accelerates loss convergence, thereby

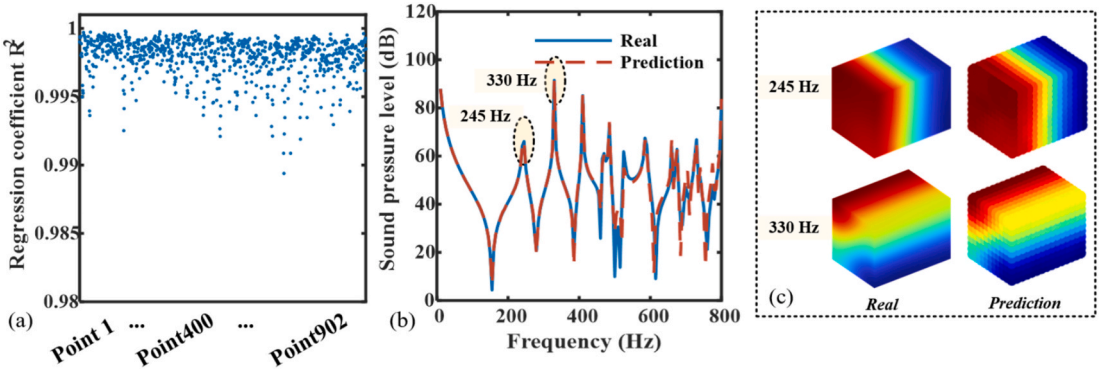

Fig. 8. Prediction effect of Net-Pre. (a) The regression coefficient R^2; (b) SPL in point (0 m, 0.15 m, 0.15 m); (c) Acoustic field distributions in 245 Hz and 330 Hz.

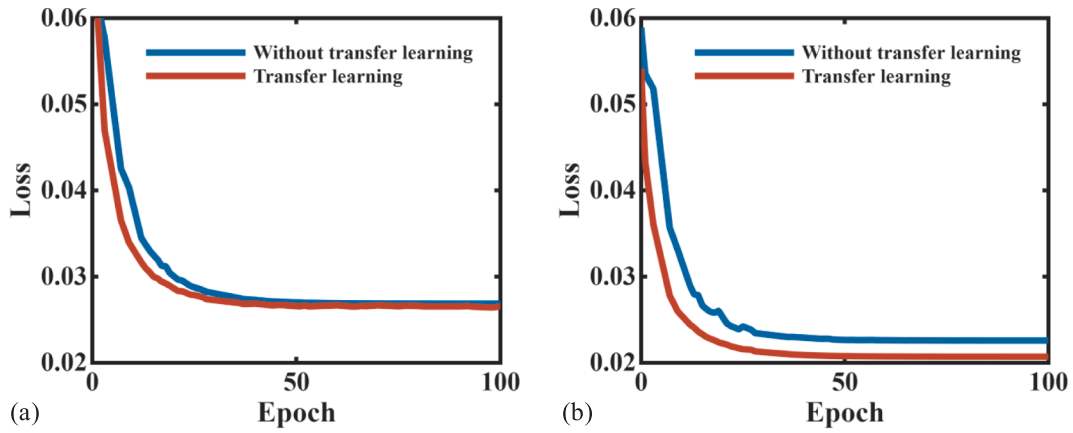

Fig. 9. Iterative plot of the loss during transfer learning training. (a) Training set; (b) Test set.

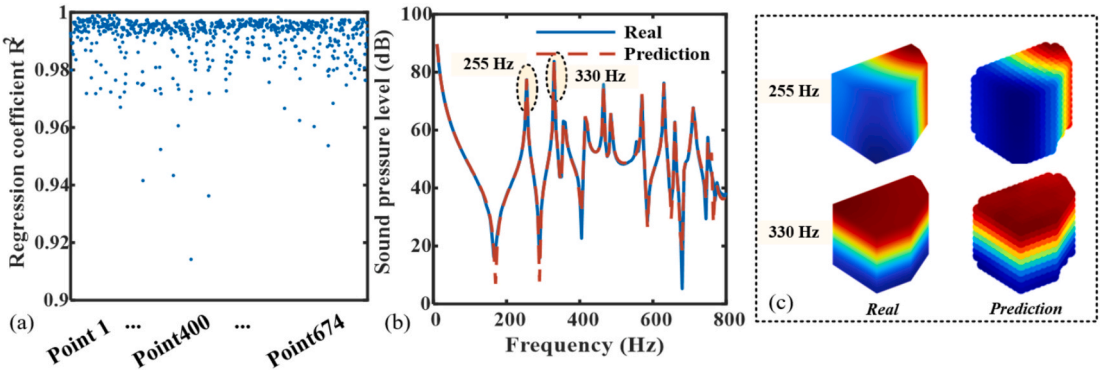

Fig. 10. Prediction effect of Net-TL. (a) The regression coefficient R^2; (b) SPL in point (0 m, 0.15 m, 0.15 m); (c) Acoustic field distribution in 255 Hz and 330 Hz.

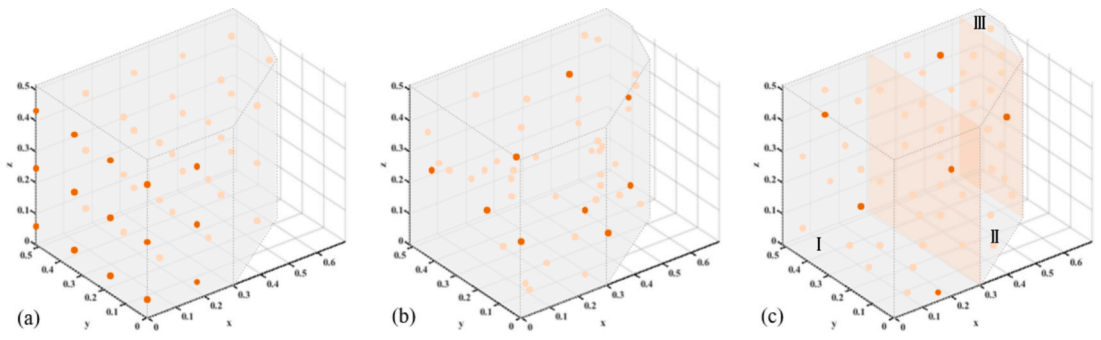

Fig. 11. Sampling strategies. (a) Ss1: uniformly distributed; (b) Ss2: randomly distributed; (c) Ss3: partitioned and randomly distributed within sub-cavities.

improving both training efficiency and predictive performance.

4.2.3. Dataset improvement

The distribution of sampling points affects the neural network's predictive performance by influencing the diversity and representativeness of the training dataset, which are crucial for capturing the system's underlying characteristics [48]. In the previous analysis, the sampling points were assumed to be uniformly distributed within the acoustic cavity and on its surface. In this section, different sampling strategies are discussed to investigate the impact of sampling point distribution on model performance. The sampling strategies used are shown in Fig. 11, with 46 sampling points selected to construct the $N/2$ dataset described in Section 4.2.2. Dark-colored points represent sampling points on the cavity surface, while light-colored points indicate sampling points inside the cavity. Specifically, sampling strategy 1 (Ss1) involves uniformly distributing sampling points within the cavity; sampling strategy 2 (Ss2) utilizes randomly distributed sampling points within the cavity; and sampling strategy 3 (Ss3) divides the acoustic cavity into three sub-cavities, with the number of sampling points in each sub-cavity proportional to its volume and randomly distributed. The number of points in each sub-cavity is listed in Table 3.

The loss iteration curves for different sampling strategies are presented in Fig. 12. Although there is no significant difference in convergence speed, the lowest loss values decrease when sampling points are randomly selected (Ss2 and Ss3). This is because that uniformly distributed sampling points may yield similar dynamic responses, resulting in a redundant dataset. Furthermore, when the dataset is constructed by partitioning the cavity into sub-cavities and randomly sampling within each region (Ss3), the prediction effect is further improved, highlighting the effectiveness of this sampling strategy. This strategy aims to prevent the random sampling points within the acoustic cavity from being clustered in a particular area. The average regression coefficients for the three sampling strategies are 0.9890, 0.9916 and 0.9925, respectively, indicating an improvement in predictive performance. Accordingly, the neural network trained with the Ss3 strategy is adopted for the TL-PTF framework in subsequent analyses.

The analysis in this section demonstrates the feasibility of applying transfer learning to sub-system modeling. In the next section, a quantitative analysis of the sampling points will be carried out through specific coupled case studies.

4.3. Coupling results

After transfer learning, the predicted transfer functions of Net-TL are employed in the TL-PTF framework for coupling analysis. The coupling responses under different cavity boundary conditions are calculated to validate the proposed method.

4.3.1. Rigid boundary

Although the performance analyses in Section 4.2 can reflect the neural network's training effect and prediction performance for subsystem responses, they do not directly indicate the prediction accuracy for the coupled system. To address this, studies are conducted on the plate-cavity coupled system in Fig. 3, where the cavity surfaces are assumed to be rigid.

Table 3
The sampling points distribution for Ss3.

Region	Count
Sub-Cavity I	21
Connection surface I-II	3
Sub-Cavity II	17
Connection surface II-III	2
Sub-Cavity III	3
Total	46

The coupling response under acoustic excitation is validated through simulation. To address this, studies are conducted on the vibro-acoustic system shown in Fig. 3. The polygonal cavity is simply connected to a 0.001 m thick aluminum plate ($E = 69$ GPa, $\mu = 0.33$, $\rho = 2730$ kg/m^3). The damping loss factor is assigned to be 0.005 for the plate while 0.001 for the cavity. The excitation point S is located at (0.15 m, 0.25 m, 0.05 m) and the listening point L is at (0.22 m, 0.22 m, 0.22 m). Based on the $\lambda_s/2$ criterion, 10 × 10 patches are selected. A plate-cavity coupled model was implemented using the multi-physics module in COMSOL®. The thin plate is simulated using the shell physics module, with its boundaries simply supported and connected to the side of the acoustic cavity. The transfer learning neural network Net-TL obtained in Section 4.2.3 was implemented in the TL-PTF method for acoustic sub-system modeling.

Fig. 13 presents the SPLs at the listening point obtained from the proposed method, as well as from simulation. The TL-PTF predictions match well with the simulation results, demonstrating the effectiveness of the proposed method. Deviations at frequencies below 30 Hz, as well as at several resonance peaks, are mainly due to the neglect of secondary acoustic feedback in the PTF formulation.

The sound field distributions corresponding to the first four peaks are presented in Fig. 14. Fig. 14(a) presents the simulation results, while Fig. 14(b) shows the predictions using the TL-PTF model, evaluated at 674 uniformly distributed sampling points on the cavity surface. At 40 Hz and 90 Hz, the system exhibits plate-dominated modes, where the plate vibration is strong and the sound pressure distribution on the coupling interface closely resembles the plate's vibration modes. At 255 Hz and 330 Hz, the system demonstrates cavity-dominated modes, where the plate vibration is relatively weak and the sound pressure distribution within the cavity displays distinct standing wave patterns. The prediction results of the TL-PTF method agree well with FEM, showing that the proposed method enables the calculation of coupling sound pressure distribution throughout the coupled system.

Furthermore, a parametric analysis is conducted by training the transfer learning neural network with varying sampling point numbers ($N_t = 45$, 30, 15, and 5, respectively). The points are randomly selected using sampling strategy 3. These neural networks are then applied within the TL-PTF framework to calculate the coupled response. Taking the SPL in Fig. 13 as a reference, Table 4 summarizes the root mean square error (RMSE) and regression coefficient R^2 for each case. To minimize the impact of sampling variability, the validation is repeated ten times and the average values are reported. When $N_t = 15$, the R^2 exceeds 0.95 and the RMSE is below 5 dB. However, when the number of sampling points is reduced to 5, the prediction performance of the TL-PTF model declines significantly. The analysis indicates that, with $N_t = 15$, the proposed TL-PTF method is sufficient for the coupled analysis of the system studied.

The current TL-PTF method requires 2.8 s to compute the overall coupled response, whereas the FEM model (with 10 elements per wavelength) takes approximately 630 s. For both the TL-PTF method and the conventional PTF method, the prediction efficiency can be evaluated by the number of repeated transfer function measurements. In the TL-PTF method, the procedure needs to be repeated $N_t = 15$ times, with excitation applied sequentially at each sampling point. By comparison, direct evaluation of the transfer functions using FEM requires repeating the procedure $N_{patch} + 1 = 101$ times, with excitation applied sequentially at the center of each patch and the excitation source point, respectively. Therefore, the TL-PTF method significantly improves efficiency by reducing the number of repeated measurements to approximately 1/7 of that required for conventional PTF method. Moreover, once the neural network is established, the TL-PTF method can be readily adapted to different patch meshes and varying excitation and listening locations, whereas the conventional PTF method typically requires repeated PTF measurements for each new configuration.

The coupling responses under point source excitation show good agreement with the simulation results. However, only the lower-order

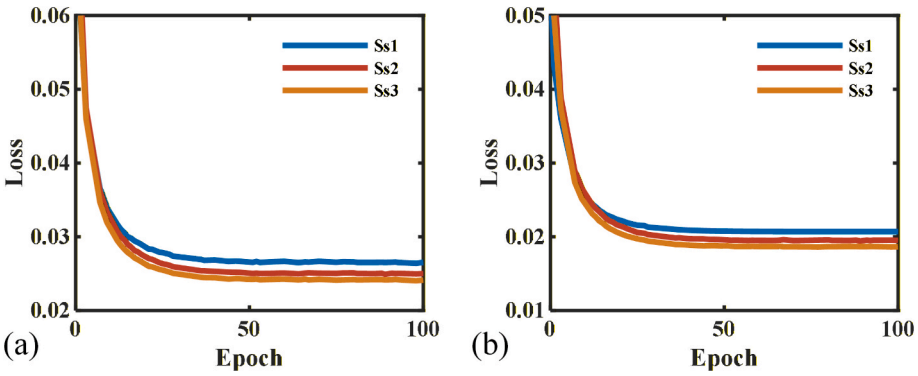

Fig. 12. Training performance of Net-TL for different sampling strategies. (a) Loss iteration for training set; (b) Loss iteration for test set.

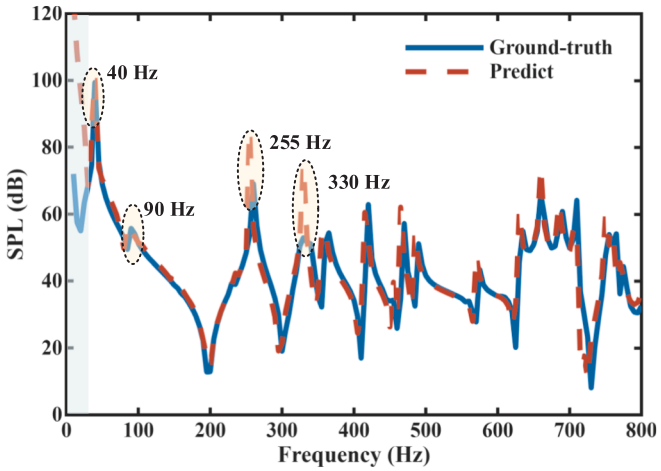

Fig. 13. The predicted SPL under acoustic excitation.

plate-governed modes are prominent in this case. To emphasize the plate-governed modes, the coupling response under force excitation was calculated and experimentally validated. The experimental setup is shown in Fig. 15. The polygonal cavity was fabricated from acrylic, with dimensions identical to those described in Section 2. The acrylic walls have a thickness of 30 mm to ensure acoustic rigidity. An aluminum plate with a thickness of 2 mm was attached to the cavity using multiple screws. A swept-sine force excitation was applied at a single point on the surface of the aluminum plate using a shaker (B&K 8200). The acoustic responses inside the cavity were measured by MEMS microphones, whose positions could be precisely adjusted using a magnetic guide rail. The force signals were measured by the force transducer on the tip of the shaker and recorded via a data acquisition (DAQ) system (NI 9234), while the audio signals were simultaneously collected by the MEMS microphones. All data were transmitted to a laptop for further analysis.

The excitation point was set at (0, $L_y/6$, $L_z/6$). Experimental results were normalized with respect to the excitation force. To represent external excitation, the unit force was applied as the blocked patch pressure on the corresponding patch, while the blocked patch pressures on all other patches were set to zero. The transfer functions were predicted using the same Net-TL model as in Section 4.3.1. The SPLs in three listening points predicted by the TL-PTF method are shown in Fig. 16 and compared with the experimental results. The predicted results agree well with the experimental data, although additional SPL peaks are observed at certain frequencies in the experimental curves, such as at

Table 4
MSE and R^2 with different number of sampling points.

N_t	RMSE (dB)	R^2
45	0.3422	0.9996
30	2.0835	0.9895
15	4.4750	0.9536
5	**18.1620**	**0.8190**

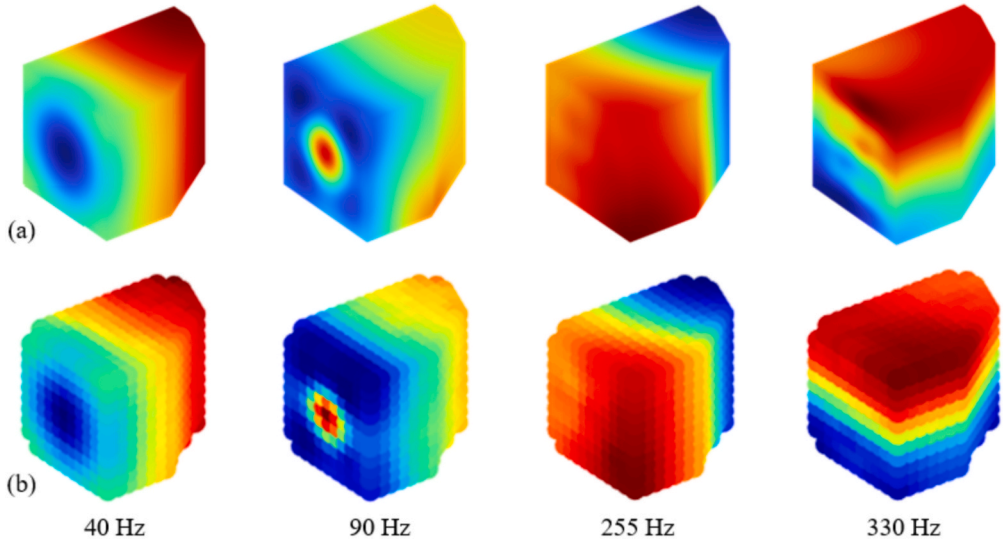

Fig. 14. Sound pressure distribution under acoustic excitation. (a) Ground-truth; (b) Predicted.

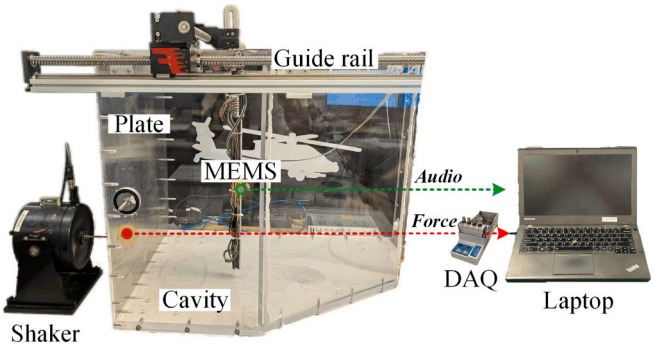

Fig. 15. The experiment setup.

200 Hz and 280 Hz. This discrepancy may be attributed to installation errors, which could introduce extra resonance and are not considered in the idealized model. Despite this, the overall agreement with the experiments is satisfactory, supporting the applicability of TL-PTF method to practical coupled problems. More accurate predictions are expected once the neural network is updated using data collected from the experimental system, which will be pursued in future work.

4.3.2. Absorptive boundaries

The plate-cavity coupling system with absorptive boundaries is considered to validate the robustness of the proposed method. The previously rigid sidewall is replaced with a porous layer with rigid backing, defined as Γ_{porous} in Fig. 17. To ensure a fair comparison, the transfer learning neural networks are trained using the same settings as in Section 4.2.3, including the network architecture, sampling strategy, and dataset size. The datasets are generated using FEM as well.

The porous layer has thickness t_p and is made of melamine foam. It is modeled in COMSOL® using the Johnson–Champoux–Allard (JCA) formulation, with the porosity of 0.99, tortuosity factor of 1, flow resistivity of 4500 Pa·s/m^2, and viscous and thermal characteristic lengths of 130 μm and 160 μm, respectively. The transferability is introduced to quantify whether the proposed TL-PTF method remains applicable under these absorptive boundary conditions, which is defined as the performance change between networks with transfer learning and without transfer learning [49]. This metric is commonly used to assess the effectiveness of transfer learning. In this study, two transferability indicators are defined based on normalized mean squared error (NMSE) and R^2 (regression coefficient), respectively:

$$\begin{cases} transfer^{-}(t_p) = \text{NMSE}_{transfer}(t_p) - \text{NMSE}_{withouttransfer}(t_p) \\ transfer^{+}(t_p) = R^2_{transfer}(t_p) - R^2_{withouttransfer}(t_p) \end{cases}. \tag{17}$$

The evaluation metrics are consistent with those used for network performance analysis in Section 4.2. With these definitions, when $transfer^{+} > 0$ and $transfer^{-} < 0$, the transfer learning strategy achieves better performance than direct training, indicating that transfer learning remains effective.

We conduct training for absorptive layer with $t_p = 0$ m, 0.02 m, 0.04 m, 0.06 m, 0.08 m, and 0.10 m. The prediction performances and transferability values are shown in Fig. 18. Fig. 18(a) and (b) present the prediction performance of the neural networks for different absorptive layer thicknesses. As the thickness increases, the network without transfer learning (blue dashed line) shows a lower NMSE and a higher R^2, indicating improved prediction performance. This can be attributed to the fact that a thicker absorptive layer introduces stronger acoustic damping at the cavity boundary, which suppresses high-frequency fluctuations in the sub-system response, making it easier for a data-driven model to learn and generalize. In comparison, the transfer learning network (red solid line) exhibits the same trend but with a much smaller variation. This is because transfer learning already

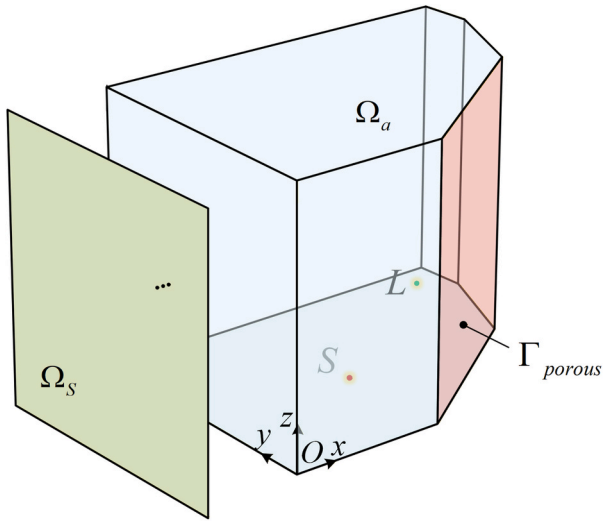

Fig. 17. The schematic diagram of the coupled system with absorptive boundary.

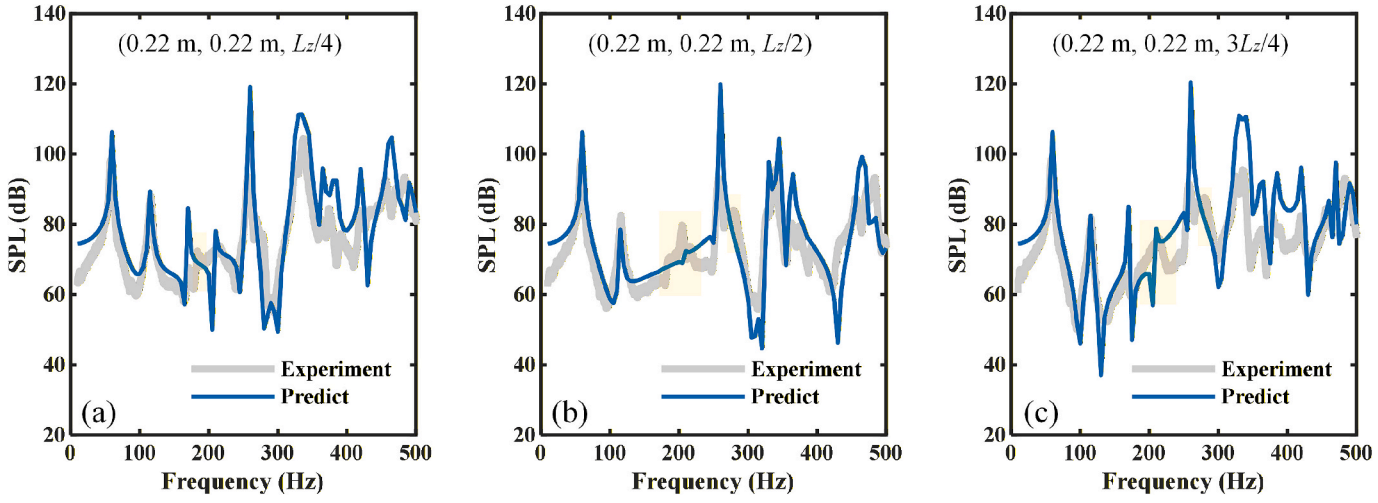

Fig. 16. Prediction result of the TL-PTF method under force excitation.

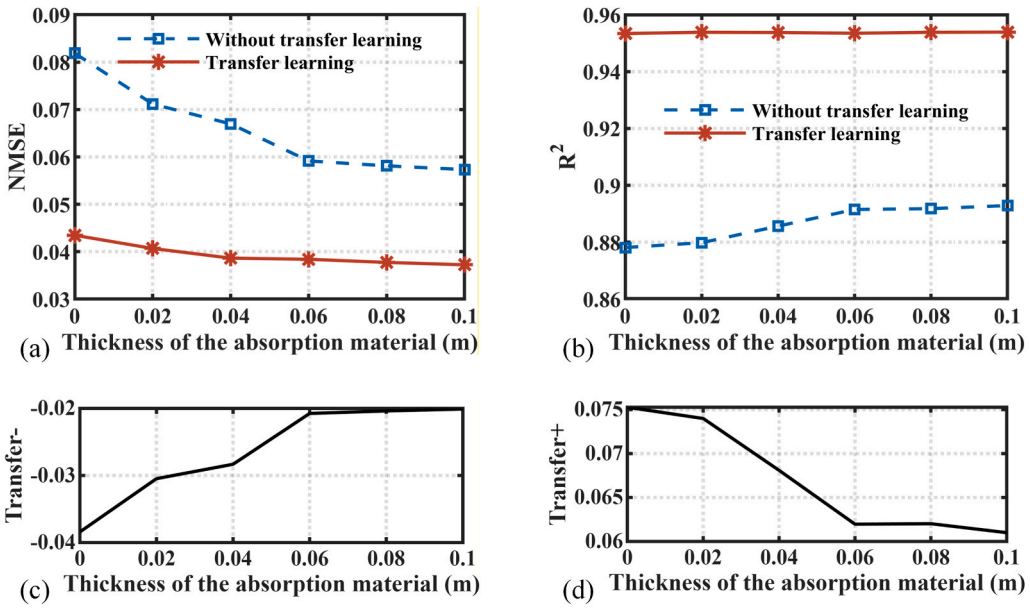

Fig. 18. The prediction performance and transferability of the neural network with different absorptive layer thicknesses.

provides a strong prior representation learned from the source domain. Therefore, the fine-tuned model remains relatively stable as the absorption layer thickness changes. Fig. 18(c) and (d) show the transferability values for different absorption layer thicknesses. Within the range investigated, *transfer*$^-$ remains negative and *transfer*$^+$ remains positive for all cases, demonstrating the effectiveness of transfer learning.

The corresponding SPLs are obtained using the TL-PTF method and compared with the FEM results, as shown in Fig. 19. The predictions of the TL-PTF method agree well with the FEM, indicating that the proposed method remains applicable under different absorptive boundary conditions.

5. Conclusion

This paper presents a rapid prediction method for the dynamic response of arbitrary structural–acoustic systems by integrating machine learning with a sub-structuring approach. A transfer learning neural network is first employed to predict the transfer functions of complex sub-systems, for which direct transfer function measurements are often time-consuming. By leveraging extensive prior knowledge from regular structures with comparable dimensions and modal characteristics, accurate predictions can be achieved using only a small amount of data from the target structure. The predicted transfer functions are then incorporated into the PTF framework to obtain the coupling responses of

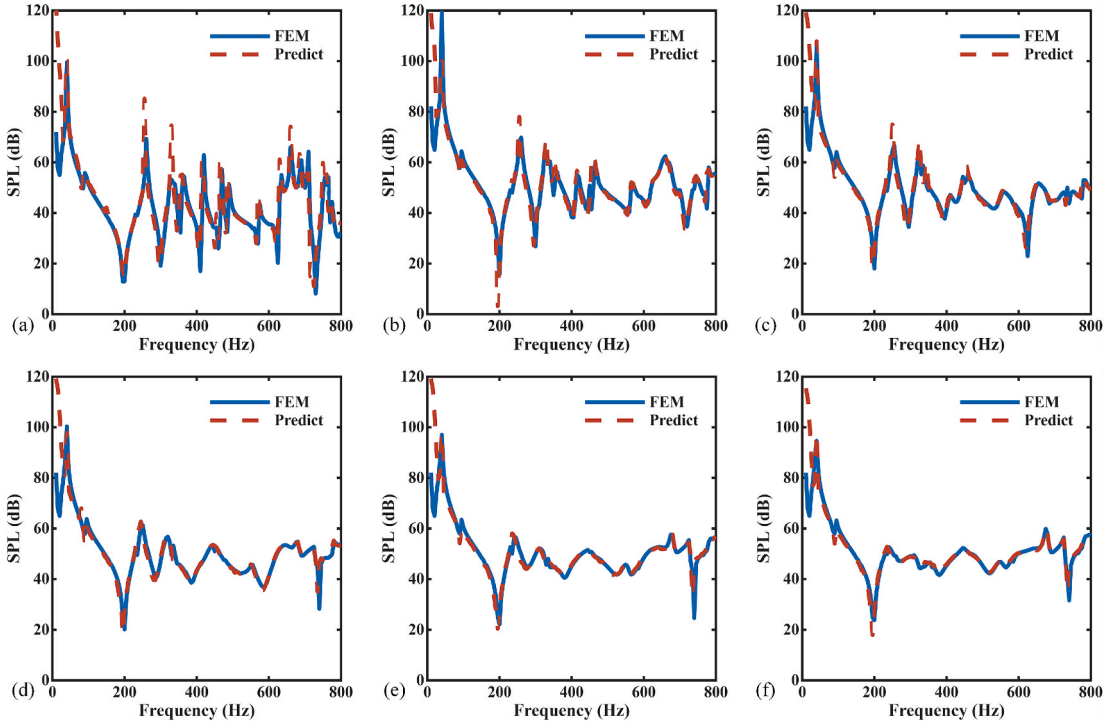

Fig. 19. The predicted SPLs with different absorptive layer thicknesses. (a) Rigid; (b) 0.02 m; (c) 0.04 m; (d) 0.06 m; (e) 0.08 m; (f) 0.10 m.

the assembled structural–acoustic systems. By constructing a neural network that learns a mapping from spatial coordinates to the transfer function, the proposed method enables efficient prediction of global responses. This enhanced PTF framework is referred to as the TL-PTF method.

The proposed method is demonstrated on a coupled plate–cavity system under different excitation locations and boundary conditions, and is validated numerically and experimentally. The results show that, with appropriate sampling strategies, the workload of the TL-PTF method is reduced to approximately 1/7 of that required by conventional patch-based approaches, while maintaining comparable accuracy. Moreover, once trained, the model remains directly applicable when the patch mesh, excitation and listening locations are modified, substantially improving both flexibility and computational efficiency in parametric studies and design optimization.

Overall, the TL-PTF method offers an efficient and practical route for structural–acoustic coupling analysis, particularly in cases where transfer functions are costly to obtain. This work provides practical guidelines for engineering applications such as cabin noise prediction. Future work will extend the approach to a wider range of structural geometries to better assess its generalizability.

CRediT authorship contribution statement

Jingjie Dong: Writing – original draft, Methodology, Investigation, Formal analysis. **Rendong Pi:** Methodology, Data curation. **Hangxing Li:** Validation, Formal analysis. **Li Cheng:** Supervision. **Xiang Yu:** Writing – review & editing, Methodology, Funding acquisition.

Declaration of competing interest

The authors declare that they have no known competing financial interests or personal relationships that could have appeared to influence the work reported in this paper.

Acknowledgement

The authors acknowledge the funding support from the Research Institute for Artificial Intelligence of Things (RIAIoT) of the Hong Kong Polytechnic University. The first author is grateful to Dr. Ng Chun-hung for his help in conducting the experiment.

Appendix A

The PTFs for thin plates are derived from the Love-Kirchhoff equation of motion (flexural vibration of thin plates)

$$-\omega^2\rho h U(x,y)+D^*\nabla^4[U(x,y)]=P(x,y), \tag{A1}$$

where $D^*=E^*h^3/12(1-\nu^2)$, and E^* is the complex Young modulus that accounts for structural damping.

The excitation term defined on patch j is given by

$$P(x,y)=\begin{cases}\dfrac{\langle F\rangle_i}{S_j} & \text{if } (x,y)\in \text{patch } j\\ 0 & \text{else}\end{cases}. \tag{A2}$$

The modal expansion of the plate's transverse displacement with simply supported boundary conditions writes

$$U(x,y)=\sum_{p,q}A_{p,q}\varphi_{p,q}(x,y,z)=\sum_{p,q}A_{p,q}\sin(k_x x)\sin(k_y y), \tag{A3}$$

where $A_{p,q}$ and $\varphi_{p,q}$ are the amplitude and mode shape function of the eigenmodes; k_x and k_y are the wavenumbers, defined as $k_x=p\pi/L_x$, $k_y=q\pi/L_y$; p and q are the modal numbers in the x- and y- directions, respectively (p, $q=0,1,2\ldots$). The same modal expansion applies to the air cavity, as given in Eq. (9).

Incorporating Eq. (A3) into Eq. (A1), and applying modes orthogonality, the modal amplitude is obtained as

$$A_{p,q}=\frac{\langle F\rangle_i\left[\int_{S_j}\varphi_{p,q}(x,y)\mathrm{d}S\right]}{S_j\left(K^*_{p,q}-\omega^2M_{p,q}\right)}, \tag{A4}$$

where $K^*_{p,q}=\int_S D^*\Phi_{p,q}\nabla^4(\varphi_{p,q})\mathrm{d}S$, $M_{p,q}=\int_S\rho h\varphi^2_{p,q}\mathrm{d}S$, and $\omega^*_{p,q}=\sqrt{\frac{K^*_{p,q}}{M_{p,q}}}$.

The PTF for plates, as defined by Eq. (1), is then obtained:

$$Y_{i,j}=\frac{\mathrm{j}\omega}{S_iS_j}\sum_{p,q}\frac{\left[\int_{S_i}\varphi_{p,q}(x,y)\mathrm{d}S\right]\left[\int_{S_j}\varphi_{p,q}(x,y)\mathrm{d}S\right]}{M_{p,q}\left[\omega^*_{p,q}-\omega^2\right]}. \tag{A5}$$

For rectangular cavities, the acoustic response due to a patch S_r with normal velocity V_n can be written as

$$A_{p,q,r}=\frac{-\int_{S_r}(\partial P/\partial n)\varphi_{p,q,r}\mathrm{d}S_r}{N_{p,q,r}(k^{*2}-k^2_{p,q,r})}=\frac{\mathrm{j}\rho_0\omega\int_{S_r}V_\mathrm{n}\varphi_{p,q,r}\mathrm{d}S_r}{N_{p,q,r}(k^{*2}-k^2_{p,q,r})}, \tag{A6}$$

where $\rho_0=1.25\ \mathrm{kg/m^3}$ is the air density.

The PTF for cavities as defined by Eq. (2) is then obtained:

$$Z_{i,j} = -j\rho\omega\sum_{p,q,r}\frac{\int_{S_i}\varphi_{p,q,r}(x_i,y_i,z_i)\mathrm{d}S_i\int_{S_j}\varphi_{p,q,r}(x_j,y_j,z_j)\mathrm{d}S_j}{(k^{*2}-k_{p,q,r}^2)N_{p,q,r}}. \tag{A7}$$

The point-to-patch transfer function and the point-to-point transfer function can be calculated by replacing the corresponding area integrals with point values.

Data availability

Data will be made available on request.

References

[1] Guy RW. Pressure developed within a cavity backing a finite panel when subjected to external transient excitation. J Acoust Soc Am 1980;68:1736–47. https://doi.org/10.1121/1.385208.

[2] Tournour M, Atalla N. Pseudostatic corrections for the forced vibroacoustic response of a structure-cavity system. J Acoust Soc Am 2000;107:2379–86. https://doi.org/10.1121/1.428624.

[3] Fahy FJ. Sound and structural vibration: Radiation, transmission and response. Elsevier; 2007.

[4] Dowell EH, Voss HM. The effect of a cavity on panel vibration. AIAA J 1963;1:476–7. https://doi.org/10.2514/3.1568.

[5] Junger MC, Feit D. Sound, structures, and their interaction. MA: MIT press Cambridge; 1986.

[6] Du JT, Li WL, Xu HA, Liu ZG. Vibro-acoustic analysis of a rectangular cavity bounded by a flexible panel with elastically restrained edges. J Acoust Soc Am 2012;131:2799–810. https://doi.org/10.1121/1.3693652.

[7] Mohamady S, Raja Ahmad RK, Montazeri A, Zahari R, Abdul Jalil NA. Modeling and eigenfrequency analysis of sound-structure interaction in a rectangular enclosure with finite element method. Adv Acoust Vib 2009;2009:371297. https://doi.org/10.1155/2009/371297.

[8] Chappell DJ, Tanner G, Giani S. Boundary element dynamical energy analysis: a versatile method for solving two or three dimensional wave problems in the high frequency limit. J Comput Phys 2012;231:6181–91. https://doi.org/10.1016/j.jcp.2012.05.028.

[9] Sun Y, Zhang G, Lee HP, Zheng H, Luo Z, Li F. Sound transmission of truss-based X-shaped inertial amplification metamaterial double panels. Int J Mech Sci 2024;283:109669. https://doi.org/10.1016/j.ijmecsci.2024.109669.

[10] Allen H. Vibro-acoustic dynamics in the presence of uncertainty and nonlinearity. Apollo - University of Cambridge Repository; 2026. 10.17863/CAM.124938.

[11] Li YY, Cheng L. Modifications of acoustic modes and coupling due to a leaning wall in a rectangular cavity. J Acoust Soc Am 2004;116:3312–8. https://doi.org/10.1121/1.1823331.

[12] Li YY, Cheng L. Vibro-acoustic analysis of a rectangular-like cavity with a tilted wall. Appl Acoust 2007;68:739–51. https://doi.org/10.1016/j.apacoust.2006.04.005.

[13] Fritze D, Marburg S, Hardtke H-J. FEM–BEM-coupling and structural–acoustic sensitivity analysis for shell geometries. Comput Struct 2005;83:143–54. https://doi.org/10.1016/j.compstruc.2004.05.019.

[14] Xuan L, Jin G, Gong J, Zhang W, Ming P. Time domain finite volume method for three-dimensional structural–acoustic coupling analysis. Appl Acoust 2014;76:138–49. https://doi.org/10.1016/j.apacoust.2013.07.024.

[15] Xie X, Zheng H, Qu Y. A variational formulation for vibro-acoustic analysis of a panel backed by an irregularly-bounded cavity. J Sound Vib 2016;373:147–63. https://doi.org/10.1016/j.jsv.2016.03.003.

[16] Sun Z, Jin G, Ye T, Yuan J. Interior vibro-acoustic modeling and modal analysis of coupled panel-cavity systems using wavelet finite-element approach. J Acoust Soc Am 2025;157:4482–501. https://doi.org/10.1121/10.0036903.

[17] Ouisse M, Maxit L, Cacciolati C, Guyader J-L. Patch transfer functions as a tool to couple linear acoustic problems. J Vib Acoust 2005;127:458–66. https://doi.org/10.1115/1.2013302.

[18] Chazot J-D, Guyader J-L. Prediction of transmission loss of double panels with a patch-mobility method. J Acoust Soc Am 2007;121:267–78. https://doi.org/10.1121/1.2395920.

[19] Maxit L, Yang C, Cheng L, Guyader J-L. Modeling of micro-perforated panels in a complex vibro-acoustic environment using patch transfer function approach. J Acoust Soc Am 2012;131:2118–30. https://doi.org/10.1121/1.3682055.

[20] Yu X, Cui FS, Cheng L. On the acoustic analysis and optimization of ducted ventilation systems using a sub-structuring approach. J Acoust Soc Am 2016;139:279–89. https://doi.org/10.1121/1.4939785.

[21] Zhang X, Cheng L. Acoustic silencing in a flow duct with micro-perforated panel liners. Appl Acoust 2020;167:107382. https://doi.org/10.1016/j.apacoust.2020.107382.

[22] Yu X, Lu Z, Cheng L, Cui F. On the sound insulation of acoustic metasurface using a sub-structuring approach. J Sound Vib 2017;401:190–203. https://doi.org/10.1016/j.jsv.2017.04.042.

[23] Li Y, Li L, Xiao L, Cheng L, Yu X. Enhancing ventilation window acoustics with sonic black hole integration: a performance evaluation. Appl Acoust 2025;229:110388. https://doi.org/10.1016/j.apacoust.2024.110388.

[24] Albert CG, Veronesi G, Nijman E, Rejlek J. Prediction of the vibro-acoustic response of a structure-liner-fluid system based on a patch transfer function approach and direct experimental subsystem characterisation. Appl Acoust 2016;112:14–24. https://doi.org/10.1016/j.apacoust.2016.05.006.

[25] Grialou M, Totaro N, Guyader J-L, Bocquillet A. Characterization of surface impedance of vibro-acoustic subdomains with experimental measurements. J Sound Vib 2019;460:114876. https://doi.org/10.1016/j.jsv.2019.114876.

[26] Luo Z, Li T, Yan Y, Zhou Z, Zha G. Prediction of sound insulation performance of aramid honeycomb sandwich panel based on artificial neural network. Appl Acoust 2022;190:108656. https://doi.org/10.1016/j.apacoust.2022.108656.

[27] Tao F, Liu X, Du H, Tian S, Yu W. Discover failure criteria of composites from experimental data by sparse regression. Compos B Eng 2022;239:109947. https://doi.org/10.1016/j.compositesb.2022.109947.

[28] Gardner GC, O'Leary ME, Hansen S, Sun JQ. Neural networks for prediction of acoustical properties of polyurethane foams. Appl Acoust 2003;64:229–42. https://doi.org/10.1016/S0003-682X(02)00089-0.

[29] Mallela UK, Upadhyay A. Buckling load prediction of laminated composite stiffened panels subjected to in-plane shear using artificial neural networks. Thin-Walled Struct 2016;102:158–64. https://doi.org/10.1016/j.tws.2016.01.025.

[30] Jiang C, Babaei M. Machine learning-based estimation of sound transmission loss in single and double-layered rectangular functionally graded plates. Eng Appl Artif Intel 2025;161:112112. https://doi.org/10.1016/j.engappai.2025.112112.

[31] Yu L, Qu Y, Ku B-H, Zhang M, Hong C-S, Lee JS, et al. Deep learning approach-based prediction of transfer functions in structure-acoustic coupling models. Results Eng 2025;28:108054. https://doi.org/10.1016/j.rineng.2025.108054.

[32] António CC, Hoffbauer LN. Uncertainty propagation in inverse reliability-based design of composite structures. Int J Mech Mater Des 2010;6:89–102. https://doi.org/10.1007/s10999-010-9123-5.

[33] Szklarek K, Gajewski J. Optimisation of the thin-walled composite structures in terms of critical buckling force. Materials 2020;13:3881. https://doi.org/10.3390/ma13173881.

[34] Liu Y, Mei Y, Chen Y, Ding B. Resolving engineering challenges: deep learning in frequency domain for 3D inverse identification of heterogeneous composite properties. Compos B Eng 2024;276:111353. https://doi.org/10.1016/j.compositesb.2024.111353.

[35] Feng J, Qiao J, Xu Q, Zhang G, Li L. Accelerated design of acoustic-mechanical multifunctional metamaterials via neural network. Int J Mech Sci 2025;287:109920. https://doi.org/10.1016/j.ijmecsci.2025.109920.

[36] Yan J, Li Y, Yin G, Lee HP, Zheng H. Inverse design of multifunctional acoustic metamaterials with ventilation and directional acoustic control. Thin-Walled Struct 2025;217:113875. https://doi.org/10.1016/j.tws.2025.113875.

[37] Dossett WC, Kim IY. Machine learning-based sound power topology optimization for shell structures. Eng Optim 2025;57:3306–26. https://doi.org/10.1080/0305215X.2024.2434188.

[38] Tsokaktsidis DE, Maeder M, Von Wysocki T, Nau C, Marburg S. Generating narrowband automotive acoustic models from measured data with artificial neural networks and bayesian optimization of hyperparameters. J Theor Comput Acoust 2025;33:2550006. https://doi.org/10.1142/S2591728525500069.

[39] Cram S, Yu J, Luegmair M, Maeder M, Marburg S. Parameter Identification of a Large-Scale Vibroacoustic Finite Element Model with a One-Dimensional Convolutional Neural Network. J Theor Comput Acoust 2024;32:2340005. https://doi.org/10.1142/S2591728523400054.

[40] Lee D, Park Y-Y. Transfer path analysis using deep neural networks trained by measured operational responses. J Mech Sci Technol 2023;37:5739–50. https://doi.org/10.1007/s12206-023-1013-5.

[41] Lee D. Estimation of substructure frequency response functions from operational responses only using a deep learning approach. J Mech Sci Technol 2025;39:3835–48. https://doi.org/10.1007/s12206-025-0608-4.

[42] Zhan H, Wang S, Yuan X, Wei Z, Wu R, Guo J. Multitask transfer-learning-based on-demand design of multifunctional metamaterial absorbers. Opt Commun 2025;595:132373. https://doi.org/10.1016/j.optcom.2025.132373.

[43] Decrop W, Deneudt K, Parcerisas C, Schall E, Debusschere E. Transfer learning for distance classification of marine vessels using underwater sound. IEEE J Sel Top Appl Earth Obs Remote Sens 2025;18:19710–26. https://doi.org/10.1109/JSTARS.2025.3593779.

[44] Xu S, Yang H, Li T, Zhang Y. Data-driven prediction of mechanical properties of 3D-printed dual-material composites based on deep transfer learning. Compos Part Appl Sci Manuf 2025;198:109083. https://doi.org/10.1016/j.compositesa.2025.109083.

[45] Cerântola P, Maxit L, Guasch O, Deng J. Coupling sonic black holes to a resonant cavity using patch transfer functions. J Sound Vib 2025;618:119316. https://doi.org/10.1016/j.jsv.2025.119316.

[46] Weiss K, Khoshgoftaar TM, Wang D. A survey of transfer learning. J Big Data 2016;3:9. https://doi.org/10.1186/s40537-016-0043-6.

[47] Pan SJ, Yang Q. A survey on transfer learning. IEEE Trans Knowl Data Eng 2010; 22:1345–59. https://doi.org/10.1109/TKDE.2009.191.
[48] Zhang G, Zheng H, Mi Y, Li F. Soundbox-based sound insulation measurement of composite panels with viscoelastic damping. Int J Mech Sci 2024;283:109663. https://doi.org/10.1016/j.ijmecsci.2024.109663.
[49] Daelemans W. Machine learning and knowledge discovery in databases: European conference, antwerp, belgium, september 15-19, 2008, proceedings, part I. Berlin/ Heidelberg, Berlin, Heidelberg: Springer; 2008.